

This is a repository copy of *Formation and evolution of post-solitons following a high intensity laser-plasma interaction with a low-density foam target*.

White Rose Research Online URL for this paper:

<https://eprints.whiterose.ac.uk/id/eprint/174306/>

Version: Published Version

---

**Article:**

Blackman, David, Adak, Amitava, Kumar Singh, Prashant et al. (9 more authors) (2021) Formation and evolution of post-solitons following a high intensity laser-plasma interaction with a low-density foam target. Plasma Physics and Controlled Fusion. 074001. ISSN 1361-6587

<https://doi.org/10.1088/1361-6587/abf85c>

---

**Reuse**

This article is distributed under the terms of the Creative Commons Attribution (CC BY) licence. This licence allows you to distribute, remix, tweak, and build upon the work, even commercially, as long as you credit the authors for the original work. More information and the full terms of the licence here:

<https://creativecommons.org/licenses/>

**Takedown**

If you consider content in White Rose Research Online to be in breach of UK law, please notify us by emailing [eprints@whiterose.ac.uk](mailto:eprints@whiterose.ac.uk) including the URL of the record and the reason for the withdrawal request.

PAPER • OPEN ACCESS

## Formation and evolution of post-solitons following a high intensity laser-plasma interaction with a low-density foam target

To cite this article: David R Blackman *et al* 2021 *Plasma Phys. Control. Fusion* **63** 074001

View the [article online](#) for updates and enhancements.












**IOP | ebooks™**

Bringing together innovative digital publishing with leading authors from the global scientific community.

Start exploring the collection—download the first chapter of every title for free.

# Formation and evolution of post-solitons following a high intensity laser-plasma interaction with a low-density foam target

David R Blackman<sup>1,4</sup> , Amitava Adak<sup>2,\*\*</sup> , Prashant K Singh<sup>2</sup> , Amit D Lad<sup>2</sup> , Gourab Chatterjee<sup>2</sup> , Christopher P Ridgers<sup>1</sup> , Dario Del Sorbo<sup>1</sup> , Raoul M G M Trines<sup>3</sup> , A P L Robinson<sup>3</sup> , Wigen Nazarov<sup>5</sup>, G Ravindra Kumar<sup>2</sup>  and John Pasley<sup>1,3,\*</sup> 

<sup>1</sup> York Plasma Institute, Department of Physics, University of York, Heslington, York YO10 5DD, United Kingdom

<sup>2</sup> Tata Institute of Fundamental Research, Dr Homi Bhabha Road, Colaba, Mumbai 400005, India

<sup>3</sup> Central Laser Facility, STFC Rutherford Appleton Laboratory, Harwell Campus, Didcot OX11 0QX, United Kingdom

<sup>4</sup> Mechanical and Aerospace Engineering, University of California San Diego, 9500 Gilman Drive, La Jolla, CA 92093-0411, United States of America

<sup>5</sup> School of Chemistry, St Andrews University, St Andrews, Fife KY16 9ST, United Kingdom

E-mail: [john.pasley@york.ac.uk](mailto:john.pasley@york.ac.uk)

Received 13 February 2021, revised 3 April 2021

Accepted for publication 15 April 2021

Published 18 May 2021



## Abstract

The formation and evolution of post-solitons has been discussed for quite some time both analytically and through the use of particle-in-cell (PIC) codes. It is however only recently that they have been directly observed in laser-plasma experiments. Relativistic electromagnetic (EM) solitons are localised structures that can occur in collisionless plasmas. They consist of a low-frequency EM wave trapped in a low electron number-density cavity surrounded by a shell with a higher electron number-density. Here we describe the results of an experiment in which a 100 TW Ti:sapphire laser (30 fs, 800 nm) irradiates a  $0.03 \text{ g cm}^{-3}$  TMPTA foam target with a focused intensity  $I_1 = 9.5 \times 10^{17} \text{ W cm}^{-2}$ . A third harmonic ( $\lambda_{\text{probe}} \simeq 266 \text{ nm}$ ) probe is employed to diagnose plasma motion for 25 ps after the main pulse interaction via Doppler-Spectroscopy. Both radiation-hydrodynamics and 2D PIC simulations are performed to aid in the interpretation of the experimental results. We show that the rapid motion of the probe critical-surface observed in the experiment might be a signature of post-soliton wall motion.

\* Author to whom any correspondence should be addressed.

\*\* Current address: Department of Physics, Indian Institute of Technology (Indian School of Mines), Dhanbad, Jharkhand 826004, India



Original Content from this work may be used under the terms of the [Creative Commons Attribution 4.0 licence](https://creativecommons.org/licenses/by/4.0/). Any further distribution of this work must maintain attribution to the author(s) and the title of the work, journal citation and DOI.

Keywords: laser plasma Interaction, laser interaction with foam, soliton formation and evolution, pump-probe Doppler spectroscopy

(Some figures may appear in colour only in the online journal)

## 1. Introduction

The hydrodynamic evolution of over-dense foams has been the subject of considerable study in the longer pulse regime (pulse duration  $> 1$  ns) and with intensities between  $10^{13-15}$  W cm $^{-2}$  (see [1–6]), the production of shock-like perturbations by ultra-short ultra-intense laser pulses is less well understood. Such phenomena could have impacts on the possible use of foams in fast particle and x-ray production [7, 8].

In this letter we present a pump( $\omega$ )-probe( $3\omega$ ) Doppler spectroscopy experiment on low-density foam targets using the UPHILL 100TW Ti-Sapphire laser system at the Tata Institute for Fundamental Research (TIFR) in Mumbai. The density of the foam target, at  $30 \times 10^{-3}$  g cm $^{-3}$ , is larger than the pump critical density of  $5.5 \times 10^{-3}$  g cm $^{-3}$ , whilst still smaller than the probe critical density of  $50 \times 10^{-3}$  g cm $^{-3}$ , so that  $n_{\text{crit}} < n_{\text{foam}} < n_{3\omega}$ .

Relativistic solitons have been studied previously theoretically [9–16] and numerically in 1D [17]. The formation and evolution of post-solitons has been discussed theoretically and numerically through the use of PIC codes [18–23]. These phenomena have been directly observed in laser-plasma experiments via proton-probing at relativistic intensities [23–26], optical self-emission and shadowgraphy [27].

Relativistic EM solitons are localised structures that can occur in collisionless plasmas. They consist of a low-frequency EM wave trapped in a low electron density cavity surrounded by a shell with a higher electron density. The relativistic electron motion is strongly coupled with the trapped electromagnetic mode, so that both particles and fields contribute equally to the total energy of the soliton [19].

Post-solitons form as a result of the formation of relativistic EM solitons in a plasma. Relativistic EM solitons form as a result of dispersion effects [9, 15, 16] due to the finite inertia of the electron and the relativistic increase in the effective mass of the electron. PIC simulations [18, 28] show EM solitons are generated in the wake [29] of an EM pulse and propagate at a velocity significantly lower than the speed of light, and with a frequency significantly lower than the local plasma frequency.

A laser pulse travelling through a region of low density plasma is susceptible to a range of instabilities which either generate reflections, or alter the frequency of the pulse itself. If these phenomena generate EM waves with frequencies corresponding to the local plasma frequency then they can become trapped. If these trapped EM waves are of a large enough amplitude the ponderomotive force pushes electrons out of regions of high field, lowering the local electron density at the centre of the pulse and raising the density around the edges of the pulse. Ion motion can be neglected during the formation of a soliton as the oscillation period of the field inside the soliton is of the order [18] of  $2\pi\omega_{\text{pe}}^{-1}$ .

The net effect of the density distortion is that the dielectric function of the plasma in the central region is significantly increased, whilst it is decreased around the edges. The decrease in the dielectric function is not only a result of the increased electron density, but also due to the increase in the electrons' Lorentz factor  $\gamma$ , in a similar manner to the relativistic self-focusing effect [27, 30].

The ions are pushed out of this region at a much lower speed by the charge separation effect of the electrons that have already exited the region. The charge separation can be significant enough to result in ion acceleration due to a coulomb explosion [20]. On the much longer timescale of ion dynamics, the soliton ceases to be a soliton, but a low frequency EM wave packet can still remain confined in the slowly expanding plasma cavity. Over time this low frequency EM structure can leak low frequency radiation [18, 20, 28] (though higher than the oscillation frequency of the EM field in the soliton) and so gradually lose energy.

The experiments described and modelled here provide some tentative further evidence of the formation and existence of such solitons as a result of high-intensity laser-plasma interaction, but also provide what may be the first direct experimental measurements of post-soliton wall ion velocities via pump-probe Doppler spectroscopy.

## 2. Foam target pump-probe experiment

The experiment was performed at the Tata Institute of Fundamental Research with a chirped-pulse-amplified 100 TW Ti:sapphire laser system, which can provide 30 fs laser pulses at a central wavelength of 800 nm. The p-polarised pump pulse has a 500 ps contrast of  $\sim 10^7$ , and is focused to a spot size of 14  $\mu\text{m}$  diameter using an  $f/3$  off-axis parabolic mirror at an angle of incidence of  $40^\circ$ . The resulting laser intensity is  $I_1 = 9.5 \times 10^{17}$  W cm $^{-2}$ .

The probe pulse is created by splitting off a small amount of the pump beam and up-shifting it to the third harmonic ( $\lambda_{\text{probe}} \simeq 266$  nm). This probe pulse is then fed through a motorised delay-stage which can delay the pulse with micrometer resolution. The probe is directed onto the target with a spot size of  $\sim 50$   $\mu\text{m}$ , at approximately  $4^\circ$  from the surface normal. The probe is centered at, and completely overlaps the pump interaction region.

The foams are formed by polymerisation *in-situ* [7] from a polymer TriMethylol Propane TriAcrylate (TMPTA, C $_{18}$ H $_{20}$ O $_6$ ). The foam has a density of 0.03 g cm $^{-3}$ , which, if fully ionised ( $\bar{Z} = 3.85$ ), gives an electron density of  $9.64 \times 10^{21}$  cm $^{-3}$  (equivalent to  $5.5n_{\text{crit}}$ ). The fully ionised electron density is smaller than the probe-critical density of  $n_{3\omega} = 1.6 \times 10^{22}$  cm $^{-3}$ , which would allow the probe pulse to pass through the foam with little or no reflection if the foam were

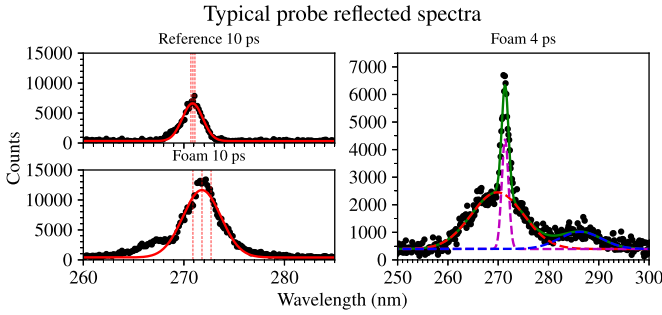


**Figure 1.** An example of several reflected probe spectra including fits used to determine the peak wavelength. The top left plot shows a reference spectrum of the probe reflecting off the frame, with a Gaussian fit (red) and vertical dashed lines indicating the peak wavelength and fitting errors. The bottom left shows the spectrum of a 10 ps delayed probe, with a gaussian fit and peak wavelength with errors. The right plot shows an example of a 4 ps delayed reflected probe spectrum with multiple peaks, the green indicates the summed peak fits, with the individual peak fits shown as dashed lines coloured red, magenta, and blue.

of a uniform density. The foam has a microscopic structure (characterised using the process described in [31]) consisting of pores  $\sim 900$  nm in size with a distance between pore centres of approximately 1400 nm.

If some of the foam were to remain intact through the pre-pulse then it is possible that the probe could interact with a plasma up to four times higher than the macroscopic density (i.e. higher than the pre-interaction average density). However, this scenario is unlikely if there is a significant compressive shock formed by the pre-pulse.

Sample results from the experiment are shown in figure 1. The probe spectrum (seen in the top left plot) has a very narrow spectral width  $\Delta\lambda = 0.9 \pm 0.2$  nm. A typical reflected spectrum of a pump-probe shot can be seen in the bottom left of figure 1. This shows a significantly wider and red-shifted peak, with an additional wider base on the shorter wavelength side of the peak. On several occasions, most notably during the experiments with a 4 ps and 10 ps delay setting, more than one peak is observed: with a wider base peak; a sharp narrow peak and a highly red-shifted smaller peak. An example of results with multiple peaked reflections is shown in the right plot of figure 1.

To obtain a value for the spectral location of each of the spectral peaks from the probe's reflected-spectra, first a noise baseline with an amplitude of  $A_b$  is fitted to the noise floor. Once the noise floor is found the data is fitted to a function of the form:

$$f(\lambda) = A_b + \sum_n A_n \exp\left(-\frac{(\lambda - \lambda_n)^2}{\sigma_n^2}\right) \quad (1)$$

where  $\lambda_n$  is the spectral location of the  $n$ th peak,  $A_n$  is the amplitude of the  $n$ th peak, and  $\sigma_n$  is the spectral width of the  $n$ th peak. An example of a fit with multiple peaks can be seen in figure 1.

At least four reflected spectra are gathered for each delay. For each foam-reflected spectrum gathered, a reflection of the

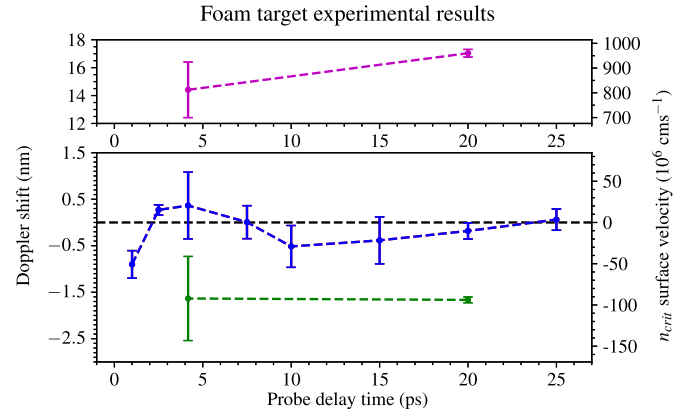


**Figure 2.** Plot of the shot-averaged Doppler shift, a blue shift (a reduction in  $\lambda$ ) would indicate a surface travelling towards the spectrometer. The results are subdivided into three sets, the blue set indicate the peaks with the least deviation from the probe wavelength, green have a large red-shift, and the magenta set have a very large blue shift. The calculated probe-surface velocity is denoted on the right hand axis of both plots. Here the positive velocity direction was chosen so that it represents material flowing towards the target surface and away from the spectrometer, while material ablating away from the target surface would have a negative velocity.

probe onto the frame housing the foams is also gathered as a reference spectrum.

In the spectra with multiple peaks the peaks can be broadly separated into three groups. The first group with a very large positive Doppler shift (12 to 18 nm, i.e. a large red-shift) corresponding to the smaller highly shifted peaks seen in figure 1. A second group with a moderately large negative Doppler shift ( $-0.76$  to  $-2.5$  nm, i.e. blue-shifted), corresponding to the smaller broad response seen in figure 1 to the left of the sharper peak. The final group which appears to follow a similar trend to earlier experiments with smaller Doppler shifts [32], corresponding to the sharp peaks seen in figure 1. To calculate the red/blue-shift of a probe-foam reflection, the spectral location of the probe-frame reflection is used as the initial wavelength, so that  $\Delta\lambda = \lambda_{\text{foam}} - \lambda_{\text{frame}}$ . All the  $\Delta\lambda$  values for each delay setting (separated into groups as appropriate) are used to calculate an average red/blue shift for each group at each delay setting. These average values are shown in figure 2.

There is a significant amount of variation in the Doppler shift of the probe reflection from shot-to-shot for the same delay setting. This shot-to-shot variation is significantly larger than both the spectral width of the peaks from the probe-reflected spectra and the error from fitting, and so the standard error from the shot-to-shot variation is used to calculate error bars for the resulting time evolution of the reflected probe Doppler-shift. Whilst the error bars shown in figure 2 are very large, there is still a visible trend: an early time outward motion of approximately  $40 \times 10^6$  cm s $^{-1}$ ; followed by an inwards motion between 2 and 6 ps (though this could vary significantly given the large variation in the data at 4 ps); and then finally an outwards motion is observed gradually falling back down towards zero velocity between 10 and 25 ps.



An additional delay setting is also used in an attempt to characterise the pre-plasma conditions, the delay stage is set to  $-20$  ps, i.e. 20 ps before the impact of the main pulse. The measured Doppler-shift of the negatively delayed probe reflection is measured at  $(0.39 \pm 0.54)$  nm with a corresponding velocity of  $(22 \pm 30) \times 10^6 \text{ cm s}^{-1}$ .

The results in blue in figure 2 are possibly Doppler-shifted as a result of a shock-like phenomena travelling through an over-dense plasma similar to that seen in solid density targets [33, 34]. However, the larger wavelength shifted results are unlikely to be the result of Doppler-shifting from reflections off moving over-critical plasma, simply due to the much larger Doppler-shifting in both cases. Whilst there is likely to be material travelling at high speeds away from the target in the blow-off region, this material is unlikely to be dense enough to affect the probe-pulse. However, depending on the scale-length and collisionality of the pre-plasma, there may be other phenomena that can account for the observed shift in wavelength.

### 3. Radiation-hydrodynamic modelling of pre-pulse absorption

The HYADES radiation hydrodynamics simulation code is used [35]. A foam with a macroscopic electron density  $n_m$  (considering the foam to be fully ionised) consists of pores which are either empty or have a density  $n_{\text{pore}} \ll n_m$  and strands with a density  $n_{\text{strand}} > n_m$ . The size of the pores and the fractal-like structure of the foam dictates the density of the strands. A more fractal-like structure will lead to narrower, denser strands. The very early time pre-pulse foam interaction will form a highly non-equilibrium plasma consisting of ablating strands and pores filled with hot low-density plasma [4]. The time taken for this plasma to equilibrate will depend on the transfer of energy from the pre-pulse through the forming plasma and how quickly a shock-like feature forms. If the plasma is under-dense for the majority of this interaction then the foam could heat volumetrically to form a large non-equilibrium plasma [2, 36].

If the target ionises quickly to an over-critical density then the heating process is likely to be dominated by the formation of a shock-like feature forming around the critical density region, similar to the behaviour seen in homogeneous targets.

At higher intensities ( $10^{13-14} \text{ W cm}^{-2}$ ) the absorption of laser light into foam targets is likely to be significantly altered, with much higher absorption than solid targets [3]. At later times, in cases with high intensity, greater penetration of the laser would lead to the formation of a cavity inside the foam [4]. It is not clear if these effects are likely to take place at the lower intensity seen in the pre-pulse ( $\sim 10^{11} \text{ W cm}^{-2}$ ) and at timescales shorter than 1 ns. With a pore-like structure on the front surface (scaled at  $\sim 900$  nm) that has a similar scale to the pump wavelength (800 nm) it is also possible that surface effects could play a part in laser absorption [37, 38].

While there are theoretical models that describe the hydrodynamic motion of foams [2] under intense laser illumination,

these are not generally implementable in standard fluid codes due to the fact they require a two-scale laser absorption model. Two such codes that have had some success at this include the 2D ALE hydro-code PALE [5] and the 1D hydro-code MULTI [6].

Since the target is  $\sim 50\%$  hydrogen atoms by number and the target has a macroscopic density  $\sim 5n_{\text{crit}}$  if fully ionised, it is possible that the target ionises quickly enough to a density  $> 2n_{\text{crit}}$  that it might be possible for the foam-like structure to behave in a similar way to a homogenous low density target.

An average-atom LTE ionisation model is used along with the polystyrene equation of state from record 7592 of the SESAME library. The multi-group radiation package is used with 100 photon groups from  $10^{-3}$ – $10^{-1}$  eV up to 10 keV, with the correct atomic ratios for the TMPTA foam. The laser solver uses parameters of  $\lambda = 800$  nm,  $\theta = 40^\circ$ , and plane polarisation, along with a pre-pulse profile consistent with experimental setup. The flux-limited thermal conductivity model is used with a flux-limiter value of 0.3. The extra transport allowed by a higher flux limiter may offer a better description of the foam target dynamics given the possibility of greater penetration by the pre-pulse laser [2].

In order to attempt modelling the foam structure a structured mesh using alternating densities between  $6 \times 10^{18} \text{ cm}^{-3}$  for  $1.2 \mu\text{m}$  and then  $4 \times 10^{18} \text{ cm}^{-3}$  for  $0.8 \mu\text{m}$  was tested against a uniform grid with a homogeneous density of  $5.4 \times 10^{18} \text{ cm}^{-3}$ . However both simulations returned almost identical simulation outputs after the very short period where the profile with alternating densities was being ionised.

To further investigate the interaction of the high-intensity pulse with the front surface pre-plasma, two separate density profiles are obtained from the HYADES output. The first density profile is obtained directly from the HYADES simulation initialised using the modulated profile at a time  $t = 490$  ps. The density profile is taken from the HYADES results 10 ps prior to the onset of the main pulse so that only the effect of the pre-pulse is taken into account. The second density profile uses a steepened version of this profile. This approach is taken as a shorter length-scale pre-plasma may be a better approximation of the density profile in the experiment. In reality the pre-plasma may have a more spherical expansion profile which is better approximated by a shorter 1D profile. This profile is calculated by making a fit to the existing density profile and reducing the characteristic length-scale  $L$ . The best fit was found using the function:

$$f(x) = a + b \exp\left(-\frac{(x-d)^{\frac{1}{2}}}{L^{\frac{1}{2}}}\right) \quad (2)$$

where  $a$  is a minimum density,  $b$  is the maximum density,  $d$  is the location of the maximum density, and  $L$  is the characteristic length-scale. This function was chosen as the much longer decay of the density from the front surface was not well represented when using a Gaussian or super-Gaussian function. The best fit to the HYADES profile gives a scale length of  $10.0 \pm 0.2 \mu\text{m}$ , the reduced profile is set to  $7 \mu\text{m}$ .

#### 4. EPOCH particle-in-cell modelling

The 1D version of the EPOCH PIC code is used [39] to model the main pulse interaction. Several simplifications are assumed for all of the PIC code simulations performed in studying the main-pulse foam-target dynamics. The first simplification is that ionisation is assumed not to have a significant effect, because the foam pre-plasma is seen in HYADES simulations, to be almost completely ionised up to the densest part of the pre-plasma shock front. The second simplification is that of using an average ion (with an atomic mass of  $7.2m_p$  and charge of  $3.85e$ ) rather than simulating multiple species of ions. This was necessary as it significantly reduced the number of particles required to achieve a convergent result. A cell size of 5 nm is used with 4000 particles per cell evenly divided between ions and electrons. (The particles referred to here are in fact macro-particles which represent ‘clouds’ of real particles. Each macro-particle being statistically weighted according to the density profile in the initial setup). Collisions are calculated using a Coulomb logarithm which is a function of the local density and temperature. The laser is set to an intensity of  $10^{18} \text{ W cm}^{-2}$  and has a gaussian temporal profile with a FWHM of 30 fs. Results from simulations using both the HYADES density profile and the shortened density profile can be seen in figure 3. Both of these plots are obtained at  $\sim 200$  fs after the reflection of the main pulse. There are two groups of velocity perturbations visible in the longer scale-length pre-plasma (see figure 3(b)): a large perturbation around the  $n_e \simeq n_{\text{crit}}/4$  and a much smaller perturbation around  $n_e \simeq n_{\text{crit}}$ . Around the same locations as both sets of velocity perturbations, are temperature peaks. Leading up to the larger of the two temperature peaks is a region of heating, which appears to be a part of the phenomenon leading up to the larger of the two velocity peaks, and will be explored in the next section.

The larger of the two sets of perturbations is visible in both the longer scale-length pre-plasma calculation (seen in figures 3(a)–(c)) and the shorter scale-length pre-plasma (seen in figures 3(d)–(f)). The smaller perturbation, located at a denser region in the longer scale-length pre-plasma, does not appear to exist in the shorter pre-plasma results. Interestingly this smaller perturbation does not appear when these simulations are run without collisions.

A hydrodynamic calculation can now be initialised by combining outputs from the EPOCH simulation above, with  $T_i$  and  $u_i$  outputs from the original HYADES calculation 10 ps prior to the main pulse. To test whether the smaller velocity perturbation (visible in the inset in figure 3(b)) is related to the phenomena observed in the experimental results, only the region between  $-10 \mu\text{m}$  and  $40 \mu\text{m}$  is simulated initially. While there is a shock formed from this perturbation, it does not travel far enough into the denser region of the pre-plasma to be seen by the  $n_{3\omega}$  probe. Also the shock front travels at a significantly smaller velocity ( $\sim 4 \times 10^6 \text{ cm s}^{-1}$ ) than any of the experimentally measured phenomena.

The outward expansion of the pre-plasma at densities greater than  $n_{\text{crit}}$ , which initially starts at  $4 \times 10^6 \text{ cm s}^{-1}$  travelling into the target, and then gradually turns into an outward

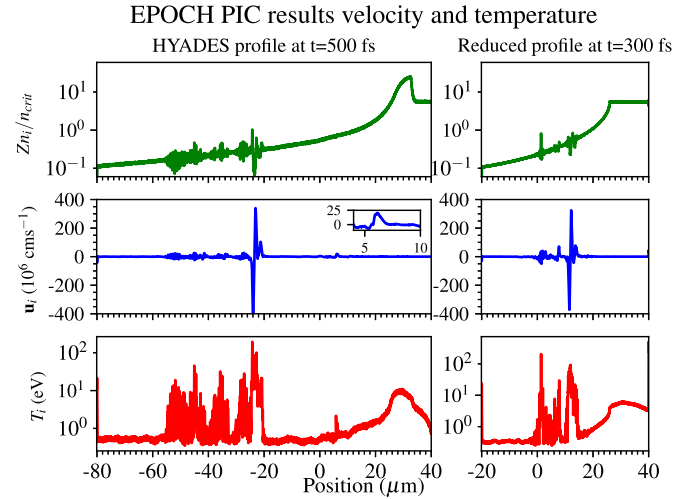


**Figure 3.** Plots showing results from EPOCH simulations using a HYADES density profile (left (a)–(c)) and a profile with a reduce density scale-length (right (d)–(f)). The top plots (a) and (d) show the ion density, the centre plots (b) and (e) show the cell-averaged fluid velocity of the ions, and the bottoms plots (c) and (f) show the cell averaged temperature. There are significant perturbations leading up to a region near  $n_{\text{crit}}/4$ , at which a large temperature spike is observable with concurring disturbances in the density and velocity plots. The inset plot highlights a comparatively small velocity perturbation of  $20 \times 10^6 \text{ cm s}^{-1}$  close to the critical density which is not observed in the shorter pre-plasma simulation. These profiles plotted here are used as the initial conditions for the hydrodynamic simulations of the shock-like perturbation after the main pulse interaction.

motion of  $2.5 \times 10^6 \text{ cm s}^{-1}$  at later times. The motion of the dense region of the target also does not appear to relate to phenomena observed in the experiment, and so further investigation into the lower density behaviour is required.

#### 5. Instability analysis

As the laser pulse travels through the under-dense plasma it suffers some significant degradation, possibly as the result of at least one plasma instability. To ascertain the nature of the instability, spectral analysis is required. Whilst both the longer and shorter scale-length simulations show significant disturbances, the longer scale-length pre-plasma is the simplest to analyse, as the instability occurs over a longer distance. The occurrence of many types of plasma instability are affected by collisions and so the analysis is performed with and without collisions switched on.

Using standard Fourier analysis techniques, pulse chirping, where the frequency or wavelength becomes a function of  $x$  or  $t$ , cannot be clearly resolved. By performing a Wigner–Ville transform on the laser pulse, rather than a Fourier transform, a determination of the wave-number  $\mathbf{k}$  as a function of  $x$  is possible. The amplitude of a particular point,  $a(x, \mathbf{k})$ , in the Wigner–Ville transform can be understood as a quasi-probability that a wave, with a wave-number  $\mathbf{k}$ , is travelling through the point at position  $x$ . The ‘quasi’ nature of the quasi-probability comes from the fact that the amplitude  $a$  is also

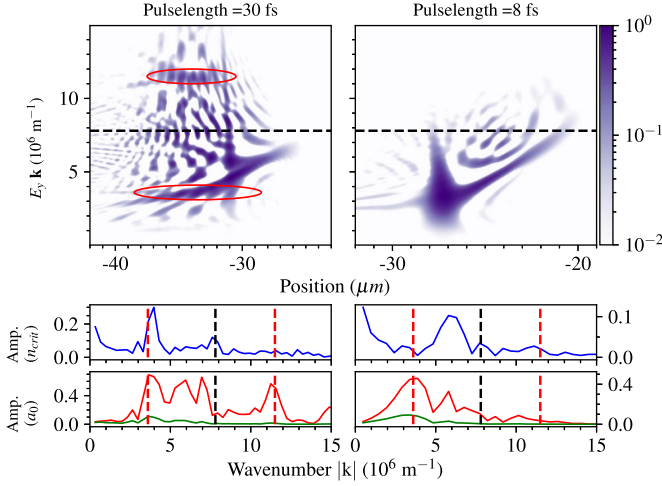


**Figure 4.** Plots from the EPOCH simulation using the HYADES density profile. The plots on the left and right show two different simulation results, the left using a laser pulse length of 30 fs, the right using a shortened pulse-length of 8 fs. The top plot shows the normalised Wigner–Ville distribution of the laser pulse at  $t = 220$  fs. The bottom set of plots shows the Fourier transform of the electron density (blue) on the top, and the forward (red) and backwards (green) travelling EM waves. Red dashed lines in the bottom plots and red ellipses denote wave-matching criteria for forward Raman scattering. The wave-number of the laser pulse in vacuum is plotted as black dashed lines in all plots.

proportional to the amplitude of the original wave at this point. The sacrifice made in this type of analysis is that the output can suffer from some interference patterns.

Figure 4 shows Wigner–Ville transforms of two different simulations with two different laser pulses, the first with  $t_{\text{pulse}} = 30$  fs, the second with a shorter,  $t_{\text{pulse}} = 8$  fs. The first simulation (figure 4, left) shows a pulse as it passes through plasma where  $n_e \sim n_{\text{crit}}/4$ . The Wigner–Ville transform of the laser pulse, 220 fs later in time, show significant disturbance of the pulse from instabilities in the plasma. The wave matching criteria for forward Raman scattering requires that the wave-number  $\mathbf{k}_s = \mathbf{k}_l \pm \mathbf{k}_{\text{pe}}$ , where the subscript  $s$  refers to a scattered wave,  $l$  refers to the incoming laser pulse, and  $\text{pe}$  refers to a co-propagating Langmuir wave. The criteria for Raman Backwards scattering requires a wave travelling in the opposing direction and has wave matching criteria of  $\mathbf{k}_s = \mathbf{k}_{\text{pe}} - \mathbf{k}_l$ . Distinguishing between these two phenomena is not always possible.

In order to determine whether forward or backward Raman scattering is dominating the interaction the forward and backwards travelling EM waves can be analysed separately by normalising to the fields  $E_p = m_e \omega_p c / e$  and  $B_p = m_e \omega_p / e$  and computing the forward propagating EM wave profile  $a_f = (E_y + B_z)$ , and  $a_b = (E_y - B_z)$ . The results from this can be seen in figure 4.

The laser pulse, when travelling through a vacuum, has a wavelength of 800 nm and so has a wave-number of  $\mathbf{k} = 7.85 \times 10^6 \text{ m}^{-1}$ . So with the forward scattering wave-matching criteria there should be scattered light wave-numbers of  $|\mathbf{k}_{f+}| \sim 12 \times 10^6 \text{ m}^{-1}$  and  $|\mathbf{k}_{f-}| \sim 4 \times 10^6 \text{ m}^{-1}$ , which are drawn on figure 4. The criteria for backwards scattering give a

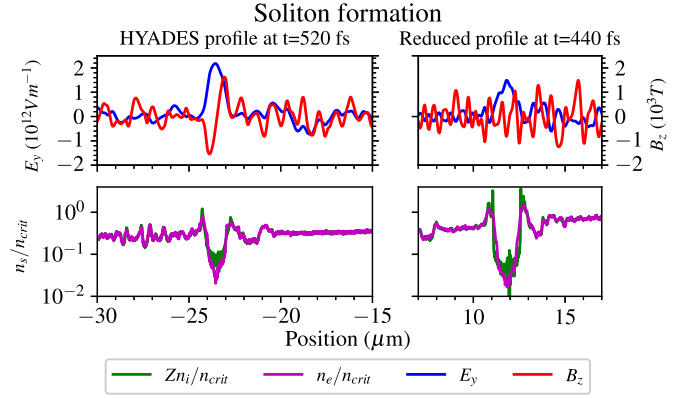


**Figure 5.** Plots from EPOCH simulations from both the longer (left) and shorter (right) pre-plasma runs. The top plots show electric and magnetic fields, whilst the bottom plots show ion ( $Zn_i/n_{\text{crit}}$ ) and electron density ( $n_e/n_{\text{crit}}$ ) around the  $n_e \sim n_{\text{crit}}/4$  region.

$|\mathbf{k}_b| \sim 4 \times 10^6 \text{ m}^{-1}$ . There is a significant peak in the Fourier transform of the electron density visible in the first simulation (bottom left of figure 4) at  $\mathbf{k}_{\text{pe}} \simeq 4 \times 10^6 \text{ m}^{-1}$  (see the bottom-right plot in figure 4) which matches part of the wave matching criteria for both of the SRS instabilities, and this signal can be attributed to a sum of both the forward and backwards Raman instabilities.

Despite the larger growth rate of backwards Raman scattering, the peak from the backwards travelling EM wave signal shown in figure 4 around  $k \simeq 4 \times 10^6 \text{ m}^{-1}$  is smaller than the forward scattering peak. This discrepancy is likely due to the fact that the growth rate for backwards Raman scattering does not take into account very short pulse lengths, while the forward Raman scattered wave travels with the laser pulse and so continues to grow.

Whilst it is possible that Raman scattering is the cause of the significant red-shifting of part of the main pulse, it may not be the sole cause. To eliminate the SRS instability a shorter pulse, shortened from 30 fs to 8 fs, can be used to see if the pulse still endures a significant amount of distortion despite insufficient time for SRS instabilities to grow. Figure 4 shows the Wigner–Ville transform of the shortened 8 fs pulse at the same point in time (220 fs) and along the same density profile as the previous pulse. The pulse undergoes a significant chirp with a large amount of the pulse red-shifted to  $\mathbf{k}_l = 5 \times 10^6 \text{ m}^{-1}$  (or  $\lambda \sim 1300$  nm), the shift in wavelength of the affected pulse equates to a critical density  $n_{\text{shift}} \sim n_{\text{crit}}/4$ . However, in this simulation the downshifted light simply reflects at the point where  $n_e = n_{\text{crit}}/4$  rather than becoming trapped in the plasma. The anomalous red-shift of the laser pulse in this case is strongly indicative of scattering due to photon acceleration [40] (or deceleration in this case) which has been previously observed in laser wake-field settings [41].

### 5.1. Soliton-like disturbance formation and evolution

The large disturbances visible in figure 3 at around the  $n_e \sim n_e/4$  regions, in both simulations are re-plotted at later times in figure 5, along with the local electric and magnetic fields.



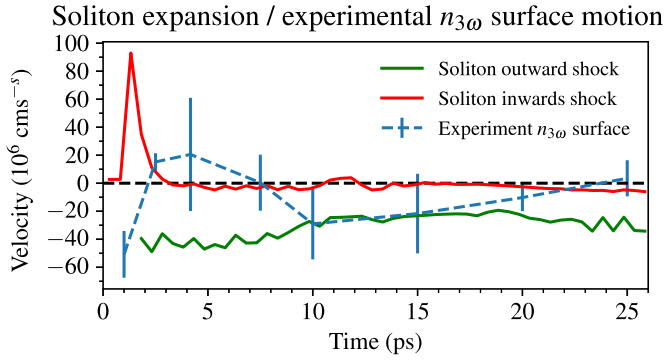


**Figure 6.** Hydrodynamic calculations of the expansion of the post-soliton like phenomena observable in the longer scale-length pre-plasma in figure 5. The green line shows the outwards motion of the shock facing away from the target bulk. The red line shows the motion of the shock on the denser side of the post-soliton, which is initially travelling towards the target bulk. These are compared to the experimentally observed  $n_{3\omega}$  surface velocities.

The phenomena observable in the longer pre-plasma simulation shows a deep depression in both the electron and ion density surrounded by denser plasma. Within the depression there is a large-amplitude oscillating electromagnetic field with the same polarisation as the laser pulse. The phenomena in the shorter pre-plasma is similar, though the magnetic field does not appear to correlate, this could be related to the expansion of post-soliton walls. This particular type of feature appears to be very similar to electromagnetic post-solitons observed in similar conditions [9, 18, 19, 25, 27]. The low density material in the central depression is surrounded by a higher density region of ejected electrons (presumably ponderomotively pushed out of the higher field region) and ions. The surrounding material is travelling at extremely high cell-averaged ion velocities; with the wall on the low density side having a velocity of  $400 \times 10^6 \text{ cm s}^{-1}$  out away from the target, and the high density wall having a velocity of  $200 \times 10^6 \text{ cm s}^{-1}$  towards the target bulk.

Calculations of the longer term evolution of these structures has been attempted using a Lagrangian hydrodynamics code, in this case simply using the PIC code ion density  $n_i$ , ion temperature  $T_i$ , and a cell averaged ion velocity  $\mathbf{u}_i$ . The density at the shock fronts,  $n_{\text{front}}$ , varies significantly, starting at  $n_{\text{front}} \leq n_{\text{crit}}$  and then rising as high as  $n_{\text{front}} \sim 4n_{\text{crit}}$ . The velocity of the walls is compared to experimental measurements in figure 6.

Whether a probe, with a critical density of  $n_{3\omega} \simeq 9n_{\text{crit}}$ , will interact with these structures depends on the evolution of the density in the shock fronts formed at the walls of the post-solitons. The shock front density depends largely on the surrounding material, as there are several smaller features that produce smaller shocks which can then merge into the post-soliton wall-shocks. The large compression of these wall-shocks is due to the initial conditions set in the fluid code from EPOCH.

The initial formation of the walls, due to ponderomotive expulsion of electrons from a region of high electric field, is

likely to be close to collisionless, due to the extremely high electron temperature in this region ( $\sim 10^5 \text{ eV}$ ).

The hydrodynamic calculation above assumes that the motion of the wall edges is a collisional hydrodynamic process rather than a collisionless one. This may not be a realistic assumption if the walls are driven by the electric field inside the soliton for a long (more than 0.5 ps) time after they are formed. In the simulations above the electric field continues oscillating inside the post-soliton cavity until the end of the PIC simulation, and so it is unclear whether the walls are driven apart by the ponderomotive force for a significant length of time or not.

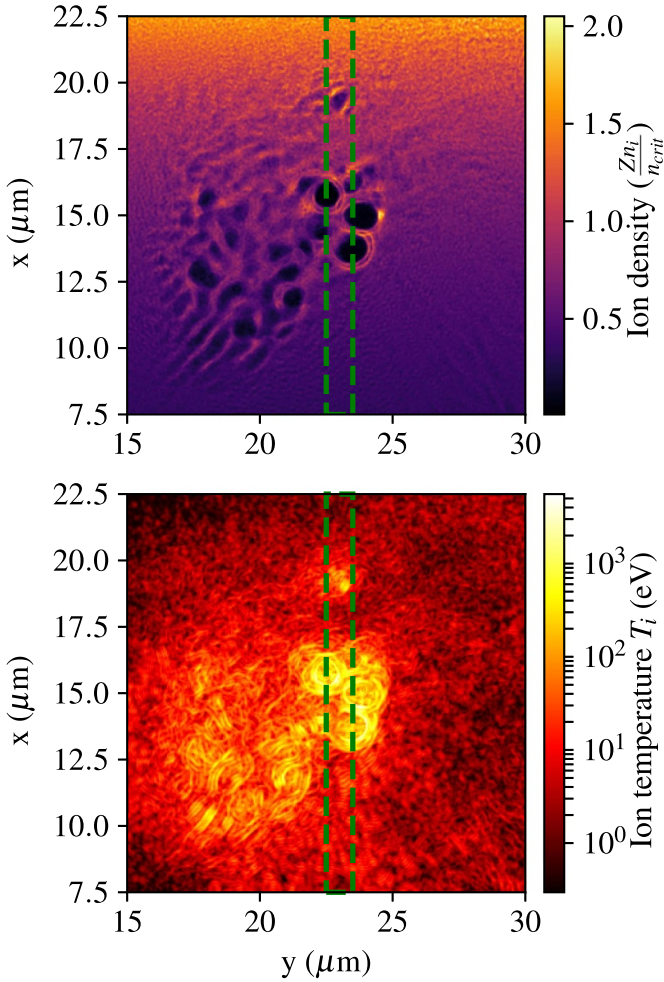
## 5.2. 2D EPOCH soliton formation

A 2D density profile can be generated by taking a 1D profile in the  $y$ -direction and copying it along the  $x$ -axis to form a shelf-like, or cliff-like, edge. While this flat-faced type of density gradient is not likely to exactly match the experimental conditions, it can be used to test whether the laser pulse will create similar structures to those seen in the 1D case, if it enters the density gradient at an angle. Two of these profiles are generated, the first profile uses the reduced scale length of  $7 \mu\text{m}$ , the second using a further reduced scale length of  $5 \mu\text{m}$ .

Two EPOCH simulations are run using the Stampede 2 cluster [42]. The first simulation consists of a  $1200 \times 2400$  grid of cells for a box with dimensions  $60 \times 120 \mu\text{m}^2$  (giving a square cell with side  $50 \text{ nm}$ ) and is run with an electron species and an average ion species ( $A = 7.2m_p$  and  $Z = 3.85$ ), 100 particles per species per cell are used and the default collision model in EPOCH is used. The laser is set with a  $\lambda = 800 \text{ nm}$  and entering the simulation box at an angle of  $40^\circ$ . The second simulation uses a slightly smaller box size of  $784 \times 1568$  maintaining the previous cell dimensions. The aforementioned density profile is used and an initial ion and electron temperature is set to zero. Initially runs with temperature profiles generated in a similar manner to the density profile are attempted, however the dynamics of the laser-plasma interaction do not change significantly and the lower signal-to-noise ratio achieved with a cold plasma are preferred. While the cell dimensions are small enough to resolve the laser wavelength adequately they will not resolve the Debye length for the higher density regions. To account for the under resolution at higher densities current smoothing and a third order spline function is used for the particle shape. No numerical heating is observable in the simulations.

**5.2.1. 2D EPOCH calculation with  $7 \mu\text{m}$  scale-length pre-plasma.** The topmost plot in figure 7 shows the ion density in the 2D EPOCH calculation approximately 200 fs after the reflection of the main pulse. The pulse reflects off a layer of plasma at  $y = 20 \mu\text{m}$ , which is the  $n_{\text{crit}}$  layer of this density gradient. In front of the critical density layer, at around  $y = 15 \mu\text{m}$  are three empty areas surrounded by denser plasma which are very similar to the post-solitons observed in the 1D calculation. However, the electric field quickly leaks out of

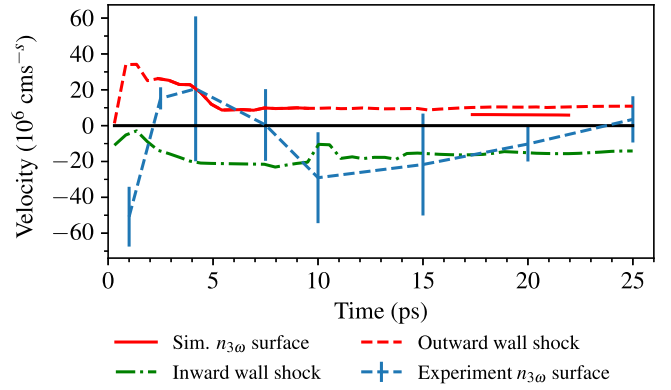
## 2D EPOCH post-soliton formation



**Figure 7.** The top plot showing the ion density profile from the 2D EPOCH calculation 200 fs after reflection of the main pulse off the  $y = 20 \mu\text{m}$  critical density layer. The bottom plot shows the ion temperature in the same region. The laser pulse would arrive from the bottom left of the picture travelling to the top right. The region marked out with green dashed lines is used for a 1D hydrodynamic calculation.

the depressions and no trapped electromagnetic radiation is observable in the soliton depressions  $\sim 50$  fs after they have formed. The ion temperature is displayed in the bottom most plot in figure 7, where it can be seen that the highest temperatures occur around the empty regions seen in the density plot at  $x = 15 \mu\text{m}$ ,  $y = 22.5 \mu\text{m}$ .

To check whether the soliton expansion shown here would give a similar velocity to those observed experimentally, a 1D Lagrangian hydrodynamics simulation is set up using a slice of data from the 2D EPOCH calculation. For the first simulation a slice is taken from the region denoted in a green box in figure 7 and an average across the  $y$ -direction is taken. The original input into the 2D EPOCH simulation did not include the pre-pulse shock front, and so there is no  $n_{3\omega}$  density surface for a probe pulse to reflect from at  $t = 0$ .

2D Soliton expansion velocity at  $n_{3\omega}$  surface motion

**Figure 8.** Plot showing the hydrodynamic evolution of the profile denoted in figure 7. The blue dashed line with error-bars shows experimental data. The solid red line indicates points in time where a  $n_{3\omega}$  surface is available for reflection. The red dashed line is the velocity of the shock closest to the dense region of the target, and the green broken line shows the velocity of the shock furthest away from the dense region of the target.

The results from this calculation can be seen in figure 8. At early times, 0–2 ps, there is no  $n_{3\omega}$  critical surface and so the routine used to calculate the Doppler shift returns zero velocity. Between 2 and 10 ps the wall-shock formed at  $X = 16 \mu\text{m}$  (see figure 8) gains significant density and so is seen by the  $n_{3\omega}$  probe. The increase in density appears to be due to two of the shock fronts briefly merging. After this time the shock front formed by the soliton wall slows down and loses density to the point where  $n_{\text{front}} < n_{3\omega}$ . Later in time, between 17 ps and 22 ps, the slower shock merges with another soliton wall ( $X = 19 \mu\text{m}$  figure 8), and is again dense enough to be seen by the  $n_{3\omega}$  probe. Also displayed in figure 8 are the outermost and innermost wall-shock velocities. While the innermost wall-shock (the wall-shock closest to, and travelling towards, the denser region of the plasma) only briefly gains enough density to be reflected by the 266 nm probe the velocity is consistent at earlier times with several of the experimentally measured points. The outermost wall-shock (the wall-shock furthest from, and travelling away from, the denser region of the plasma) shows similar velocities to the experimental results at later times but does not merge with any other shocks and so does not gain enough density to be reflected by the probe pulse.

**5.2.2. 2D EPOCH calculation with  $5 \mu\text{m}$  scale-length pre-plasma.** The second 2D EPOCH simulation, run with a shorter pre-plasma scale length of  $5 \mu\text{m}$ , shows significantly altered structures at a slightly denser region. Instead of three smaller soliton-like features, a single similar feature is observable, see figure 9 at  $x = 0 \mu\text{m}$ ,  $y = -25 \mu\text{m}$ . Similarly to the previous, longer-scale length, case the ion temperature is high in a very localised region where the soliton-like depression occurs. Profiles for a 1D hydrodynamic calculation are obtained from the 2D simulation in the same way as for the previous 2D EPOCH calculation, and the results are plotted in

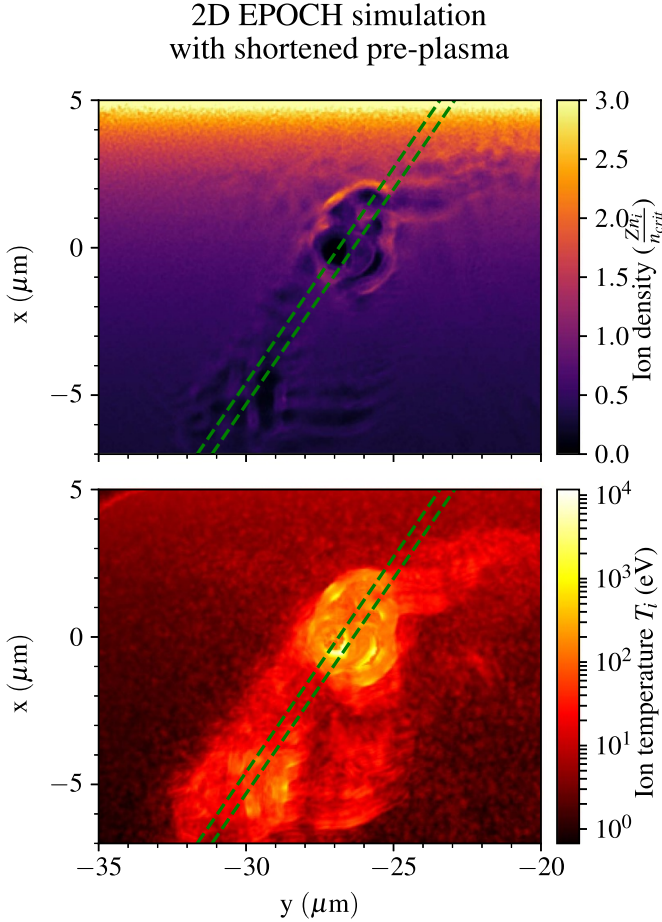


**Figure 9.** Plots showing profiles from second 2D EPOCH calculation 200 fs after the main pulse reflection off the  $y = 2 \mu\text{m}$  critical density layer. The top plot showing the ion density, the bottom plot showing the ion temperature. Similar to the previous calculations a deep depressions in ion density can be seen at around  $y = 27, x = 0 \mu\text{m}$ . The region marked out with green dashed lines is used for a 1D hydrodynamic calculation.

figure 10. The first observation to note is that there is only one large depression visible in this simulation, while there are three in the longer scale-length case. The hydrodynamic simulation for this case did not show any density surface dense enough to reflect the probe pulse. The velocity of both the innermost and outermost wall shocks did however match some of the experimentally measured velocities.

## 6. Discussion

### 6.1. 1D modelling of main pulse interaction

A large amount of energy appears to go into laser-plasma instabilities observable in the PIC code results. Both of the observed instabilities, the possible stimulated Raman scattering instability, and the photon acceleration or self-focusing red-shifting of the laser pulse, generate post-soliton-like phenomena. These post-solitons generate large shocks at their edges in the low-density regions of the pre-plasma. These wall-shocks progress at velocities comparable to those

### Soliton wall shock velocity from 2D profile with shortened pre-plasma

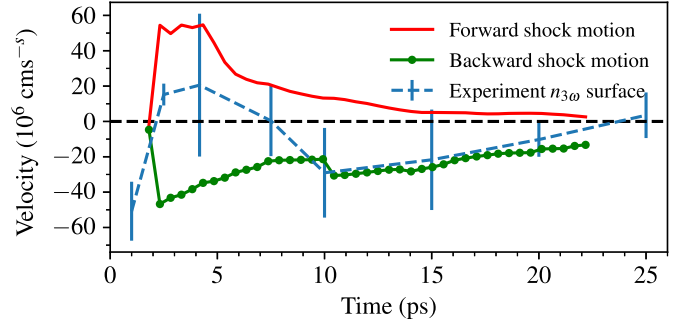


**Figure 10.** Plot showing the hydrodynamic evolution of the profile denoted in figure 9. The blue dashed line with error-bars shows experimental data. The red dashed line is the velocity of the shock closest to the dense region of the target, and the green broken line shows the velocity of the shock furthest away from the dense region of the target.

measured in the experiment (see figure 6). However, hydrodynamic calculations of the progress of these shocks show that they do not progress deep enough into the target to reach the densities observable by the probe. An alternative method of modelling the pre-pulse interaction may give a different shaped pre-plasma which may enable these shocks to progress further into the target and thus still offer a possible explanation of the cause of the Doppler shifts seen in the experiment.

### 6.2. 2D modelling of main pulse interaction

The laser-plasma interaction in the 2D case generates more post-soliton like structures around the  $n_{\text{crit}}/4$  region. The hydrodynamic motion of the wall-shocks surrounding the post-solitons are similar, in both timing and velocity, to the inward velocities measured in the experiment. However they only reach appropriate densities that will reflect a  $3\omega$  probe pulse under specific circumstances. The circumstance require that there is more than one post-soliton like depression so that the wall-shocks from one post-soliton can interact with another, and so boost the density to a high enough level to reflect the probe pulse.

No evidence of motion at sufficient velocities to explain the experimental results were observable in the very dense region ( $\gg n_{\text{crit}}$ ) of the target. This leaves only the dynamics at lower densities able to provide an explanation, even though it is a tentative one.

### 6.3. Conclusions

The extra reflected peaks recorded in the experimental results, (see figure 2) do not seem to match any phenomena occurring in either the HYADES or the EPOCH calculations and so no explanation can be made about the possible origins of these points. However, a possible explanation of the central larger Doppler shifted peaks can be made using the modelling shown here.



Post-soliton wall-shock motion might explain the inward motion into the target measured in the experiment (the positive velocities observed in figure 2). Electron heating of the pre-pulse formed shock, which explains the initial outward motion in the high contrast silicate target experiment, does not appear to explain the outward motion in this case. Looking at figure 6 it is possible that the initial outward expansion could come from an outward travelling wall-shock from a post-soliton-like phenomena, if the soliton can be formed in a region with a high enough initial density. However at later times, these outwards travelling wall-shocks would travel into less dense regions and so would be unlikely to account for later experimental results. These measurements not only support the earlier proton radiographic [24–26] and optical measurements [27] in providing evidence of soliton formation in intense laser-plasma interactions, they also provide what may be the first direct measurement of ion-velocities in such post-soliton wall plasmas.










### Data availability statement

The data that supports the findings of this study is available from the corresponding author upon reasonable request.

### Acknowledgment

J P would like to acknowledge the Engineering and Physical Science Research Council's Grant No. EP/I030018/1, A P L R would also like to acknowledge the European Research Council's STRUCMAGFAST Grant No. ERC-StG-2012 and D B would like to acknowledge the Engineering and Physical Science Research Council's Grant No. EP/K504178/1. G R K acknowledges partial support from the J C Bose Fellowship Grant No. JCB-037/2010 (Science and Engineering Research Board, Government of India). The authors are grateful for the use of computing resources provided by Science and Technology Facilities Council's e-Science facility. This research was supported in part by The National Science Foundation USA (PHY 1903098). This work used the Extreme Science and Engineering Discovery Environment (XSEDE), which is supported by National Science Foundation Grant No. ACI-1548562.

### ORCID iDs

David R Blackman  <https://orcid.org/0000-0001-7852-4216>  
 Amitava Adak  <https://orcid.org/0000-0003-0687-2830>  
 Prashant K Singh  <https://orcid.org/0000-0003-3748-5411>  
 Amit D Lad  <https://orcid.org/0000-0002-2672-1928>  
 Gourab Chatterjee  <https://orcid.org/0000-0002-0972-6452>  
 Christopher P Ridgers  <https://orcid.org/0000-0002-4078-0887>  
 Dario Del Sorbo  <https://orcid.org/0000-0003-0390-7540>  
 Raoul M G M Trines  <https://orcid.org/0000-0003-2553-0289>  
 A P L Robinson  <https://orcid.org/0000-0002-3967-7647>

G Ravindra Kumar  <https://orcid.org/0000-0002-2324-2825>

John Pasley  <https://orcid.org/0000-0001-5832-8285>

### References

- [1] Kapin T, Limpouch J and Liska R 2006 Hydrodynamic simulations of laser interactions with low-density foams *Czech. J. Phys.* **56** 493–9
- [2] Gus'kov S Y and Rozanov V B 1997 Interaction of laser radiation with a porous medium and formation of a nonequilibrium plasma *Quantum Electron.* **27** 696–701
- [3] Gus'kov S Y, Caruso A, Rozanov V B and Strangio C 2000 Interaction of a high-power laser pulse with supercritical-density porous materials *Quantum Electron.* **30** 191–206
- [4] Caruso A, Strangio C, Gus'kov S Y and Rozanov V B 2000 Interaction experiments of laser light with low density supercritical foams at the AEEF ABC facility *Laser Part. Beams* **18** 25–34
- [5] Velechovsky J, Limpouch J, Liska R and Tikhonchuk V 2016 Hydrodynamic modeling of laser interaction with micro-structured targets *Plasma Phys. Control. Fusion* **58** 095004
- [6] Cipriani M, Gus'kov S, Angelis R D, Andreoli P, Consoli F, Cristofari G, Giorgio G D, Ingenito F and Rupasov A 2016 Powerful laser pulse absorption in partly homogenized foam plasma *J. Instrum.* **11** C03062
- [7] Iwawaki T *et al* 2014 Collimated fast electron beam generation in critical density plasma *Phys. Plasmas* **21** 113103
- [8] Li Y T *et al* 2005 Demonstration of bulk acceleration of ions in ultraintense laser interactions with low-density foams *Phys. Rev. E* **72** 066404
- [9] Kozlov V A, Litvak A G and Suvorov V 1979 Envelope solitons of relativistic strong electromagnetic waves *Sov. Phys. JETP* **49** 75–80
- [10] Farina D and Bulanov S V 2001 Relativistic electromagnetic solitons in the electron-ion plasma *Phys. Rev. Lett.* **86** 5289–92
- [11] Farina D, Lontano M and Bulanov S 2000 Relativistic solitons in magnetized plasmas *Phys. Rev. E* **62** 4146–51
- [12] Esirkepov T Z, Kamenets F F, Bulanov S V and Naumova N M 1998 Low-frequency relativistic electromagnetic solitons in collisionless plasmas *J. Exp. Theor. Phys. Lett.* **68** 36–41
- [13] Kurki-Suonio T, Morrison P J and Tajima T 1989 Self-focusing of an optical beam in a plasma *Phys. Rev. A* **40** 3230–9
- [14] Gersten J I and Tzoar N 1975 Propagation of localized electromagnetic pulses in plasmas *Phys. Rev. Lett.* **35** 934–7
- [15] Tsintsadze N L and Tskhakaya D D 1977 On the theory of electrosound waves in a plasma *Sov. Phys. JETP* **4** 252–5
- [16] Kaw P K, Sen A and Katsouleas T 1992 Nonlinear 1D laser pulse solitons in a plasma *Phys. Rev. Lett.* **68** 3172–5
- [17] Sentoku Y *et al* 1999 Bursts of superreflected laser light from inhomogeneous plasmas due to the generation of relativistic solitary waves *Phys. Rev. Lett.* **83** 3434–7
- [18] Naumova N M, Bulanov S V, Esirkepov T Z, Farina D, Nishihara K, Pegoraro F, Ruhl H and Sakharov A S 2001 Formation of electromagnetic postsolitons in plasmas *Phys. Rev. Lett.* **87** 185004
- [19] Liu Y, Klimo O, Esirkepov T Z, Bulanov S V, Gu Y, Weber S and Korn G 2015 Evolution of laser induced electromagnetic postsolitons in multi-species plasma *Phys. Plasmas* **22** 112302
- [20] Esirkepov T, Nishihara K, Bulanov S V and Pegoraro F 2002 Three-dimensional relativistic electromagnetic subcycle solitons *Phys. Rev. Lett.* **89** 275002

- [21] Sánchez-Arriaga G and Lefebvre E 2011 Two-dimensional s-polarized solitary waves in plasmas. II. Stability, collisions, electromagnetic bursts and post-soliton evolution *Phys. Rev. E* **84** 036404
- [22] Sánchez-Arriaga G, Siminos E, Saxena V and Kourakis I 2015 Relativistic breather-type solitary waves with linear polarization in cold plasmas *Phys. Rev. E* **91** 033102
- [23] Borghesi M *et al* 2002 Macroscopic evidence of soliton formation in multiterawatt laser-plasma interaction *Phys. Rev. Lett.* **88** 135002
- [24] Romagnani L *et al* 2010 Observation of magnetized soliton remnants in the wake of intense laser pulse propagation through plasmas *Phys. Rev. Lett.* **105** 1–4
- [25] Sarri G *et al* 2010 Observation of postsoliton expansion following laser propagation through an underdense plasma *Phys. Rev. Lett.* **105** 175007
- [26] Sarri G *et al* 2011 Observation of plasma density dependence of electromagnetic soliton excitation by an intense laser pulse *Phys. Plasmas* **18** 080704
- [27] Zhu B, Wu Y C, Dong K G, Hong W, Teng J, Zhou W M, Cao L F and Gu Y Q 2012 Observation of a strong correlation between electromagnetic soliton formation and relativistic self-focusing for ultra-short laser pulses propagating through an under-dense plasma *Phys. Plasmas* **19** 102304
- [28] Bulanov S V, Esirkepov T Z, Naumova N M, Pegoraro F and Vshivkov V A 1999 Solitonlike electromagnetic waves behind a superintense laser pulse in a plasma *Phys. Rev. Lett.* **82** 3440–3
- [29] Bulanov C V, Esirkepov T Z, Kamenets F F and Naumova N M 1995 Electromagnetic soliton formation during interaction of relativistically strong laser-pulses with plasmas *Plasma Phys. Rep.* **21** 550–61
- [30] Kaw P, Schmidt G and Wilcox T 1973 Filamentation and trapping of electromagnetic radiation in plasmas *Phys. Fluids* **16** 1522–5
- [31] Faith D, Horsfield C J and Nazarov W 2006 Characterization of pore size of trimethylol propane triacrylate (TMPTA) polymer foam by pulsed sputter coating and SEM analysis *J. Mater. Sci.* **41** 3973–7
- [32] Mondal S, Lad A D, Ahmed S, Narayanan V, Pasley J, Rajeev P P, Robinson A P L and Kumar G R 2010 Doppler spectrometry for ultrafast temporal mapping of density dynamics in laser-induced plasmas *Phys. Rev. Lett.* **105** 105002
- [33] Adak A, Blackman D R, Chatterjee G, Kumar Singh P, Lad A D, Brijesh P, Robinson A P L, Pasley J and Kumar G R 2014 Ultrafast dynamics of a near-solid-density layer in an intense femtosecond laser-excited plasma *Phys. Plasmas* **21** 062704
- [34] Adak A, Singh P K, Blackman D R, Lad A D, Chatterjee G, Pasley J, Robinson A P L and Ravindra Kumar G 2017 Controlling femtosecond-laser-driven shock-waves in hot, dense plasma *Phys. Plasmas* **24** 072702
- [35] Larsen J T and Lane S M 1994 HYADES-a plasma hydrodynamics code for dense plasma studies *J. Quant. Spectrosc. Radiat. Transfer* **51** 179–86
- [36] Gus'kov S Y, Limpouch J, Nicolai P and Tikhonchuk V T 2011 Laser-supported ionization wave in under-dense gases and foams *Phys. Plasmas* **18** 103114
- [37] Rajeev P, Taneja P, Ayyub P, Sandhu A and Kumar G 2003 Metal nanoplasmas as bright sources of hard x-ray pulses *Phys. Rev. Lett.* **90** 115002
- [38] Kahaly S, Yadav S K, Wang W M, Sengupta S, Sheng Z M, Das A, Kaw P K and Kumar G R 2008 Near-complete absorption of intense, ultrashort laser light by sub- $\lambda$  gratings *Phys. Rev. Lett.* **101** 3–6
- [39] Arber T D *et al* 2015 Contemporary particle-in-cell approach to laser-plasma modelling *Plasma Phys. Control. Fusion* **57** 113001
- [40] Mendonça J T and Bingham R 2015 Photon acceleration as a scattering process *Plasma Phys. Control. Fusion* **57** 044011
- [41] Murphy C D *et al* 2006 Evidence of photon acceleration by laser wake fields *Phys. Plasmas* **13** 033108
- [42] Towns J *et al* 2014 XSEDE: accelerating scientific discovery *Comput. Sci. Eng.* **16** 62–74